

量子幫浦效應、雜訊分析及電子失相行為於低維度傳輸系統

研究生：鐘淑維

指導教授：張俊彥 院士

朱仲夏 教授

國立交通大學

電子工程學系 電子研究所博士班

中文摘要

本論文的研究是針對目前幾個低維度系統的重要議題做探討。首先，我們研究單電子式 Mach-Zehnder (MZ) 及雙電子式 Hanbury Brown Twiss (HBT) 干涉儀的電流及雜訊的能見度，並操作在量子霍爾效應的狀態下。於 HBT 干涉儀中，電流並沒有 Aharonov-Bohm 振盪，唯一能跟 MZ 干涉儀比較的物理量只有雜訊。MZ 干涉儀的雜訊包含兩個部分： h/e 及 $h/2e$ 振盪， $h/2e$ 振盪因溫度、偏壓及失相率的影響而減少比 h/e 振盪更快。另一方面，HBT 干涉儀的雜訊只包含 h/e 振盪。由直覺的想法會認為雙電子式 HBT 干涉儀的雜訊特性與 MZ 干涉儀中的 $h/2e$ 雜訊振盪(雙粒子效應)有密切相關，然而，結果顯示電子式干涉儀的特性是由電子圍繞磁通量的圈數決定，與粒子數多寡無關，所以 HBT 干涉儀的 h/e 雜訊振盪特性與 MZ 干涉儀中的 $h/2e$ 雜訊振盪特性相似。

接下來我們偏離穩態系統，轉而研究電流及雜訊於量子幫浦所驅動之 MZ 干涉儀。MZ 干涉儀的兩 AC 分束電閘不僅可調整電子的穿透係數並可驅動電子的

流動。相對於傳統的偏壓驅動之 MZ 干涉儀，電流的產生純粹於量子效應，其包含了磁通量無關部分 $I^{(0)}$ 及相關部分 $I^{(\Phi)}$ 。這兩個部份隨著頻率的變化與兩個時間尺度有關，也就是平均傳輸時間及兩臂傳輸時間差。另一方面， $I^{(0)}$ 的震盪振幅隨著頻率增加而增加，而 $I^{(\Phi)}$ 的震盪振幅並不隨頻率改變。溫度效應以指數率快速地減少 $I^{(\Phi)}$ 乃因干涉儀的兩臂非等長。當 MZ 干涉儀的兩分束電閘有相等的穿透係數時，困擾實驗的整流效應變得不再影響系統，也就是此時所量到物理量為純量子幫浦效應。此外，我們探討失相效應於長鬆散時間狀態及短鬆散時間狀態。於這兩種狀態下，電流的磁通量相關部份會因失相因子強度增加而被消滅，而電流的磁通量無關部份之消滅情形只發生於長鬆散時間狀態。

此外，於 MZ 干涉儀中，不同於電流的是雜訊值總為負值，此為費米子的特性之一。此部分，我們專注雜訊值於低溫及低頻兩個狀態。於低溫的狀態，雜訊的振幅隨著頻率的增加而上升，因著電流及雜訊隨著頻率呈現不同的變化，使得有些區域電流雖為零但是雜訊仍然存在，近一步觀察低頻極限，我們發現無雜訊區可經由調整磁相位及幫浦相位而得之。另一考量，也就是低頻狀態，無雜訊區亦可經由同樣的方法而得，然而溫度的出現，使得雜訊值不再消失。

最後，我們研究量子閘極陣列式幫浦，其結構為一對指狀金屬閘極交錯排列於量子線上，閘極均 AC 偏壓，其保持頻率相同但有相位差。當每陣列的指狀閘極數大於二時，電流的產生轉為因時變 Bragg 反射機制的發生，而不再是光子通道間干涉引起。這樣的解釋可適用於瞬時及非瞬時狀態。

Topics in the Low Dimensional Systems: Effects of Quantum Pumping, Shot Noise and Decoherence

Student: Shu-Wei Vanessa Chung Advisors: Prof. Chun-Yen Chang

Prof. Chon-Saar Chu

A Dissertation

Department of Electronics Engineering and Institute of Electronics

National Chiao Tung University, Hsinchu, Taiwan, R. O. C.



We have investigated the important issues in several low dimensional systems. First, we study the visibilities of the current and the shot noise in the one-particle Mach-Zehnder (MZ) and two-particle Hanbury Brown Twiss (HBT) interferometers. Both electronic systems are implemented in the quantum Hall regime. The possible comparisons between two interferometers are only through the shot noise due to the absence of the Aharonov-Bohm oscillations in the currents of HBT interferometers. The shot noises of MZ interferometers are composed of h/e and $h/2e$ oscillations. The visibilities of $h/2e$ oscillations are decreased with the temperature, the voltage and the dephasing faster than those of h/e oscillations. In the other hand, the shot noises of

HBT interferometers only have h/e oscillations. Unlike the naive intuitions that the properties of shot noises of two-particle HBT interferometers would be related to the two particle effects of $h/2e$ oscillations of MZ interferometers, it is the number of enclosing flux deciding the properties of visibilities, not particle numbers. The variations of h/e oscillations with system parameters in HBT interferometers are similar to those of h/e oscillations of MZ interferometers.

Away from the stationary setups, we study the currents and the shot noises in quantum pump driven MZ interferometers. Two AC beam splitters of MZ interferometers are applied to modulate the electron transmissions and excite the electron flows. Contrary to the voltage driven MZ interferometers, the pump currents composed of the flux-independent part $I^{(0)}$ and the flux-dependent part $I^{(\Phi)}$ are arose from pure quantum effects. Subject to the pump frequency, the oscillations of both parts of currents are related to two time scales, average arm traversal time and the difference of two arm traversal times. In the other hand, the amplitudes of oscillations in $I^{(0)}$ increase with frequency; the amplitudes of oscillations in $I^{(\Phi)}$ are kept constant. The temperature effects only smear $I^{(\Phi)}$ exponentially as a results of the arm asymmetry. The rectification effects could be annihilated as the semi-transparence of beam splitters, i.e. the availability of the true pump currents in MZ interferometers. The effects of the decoherence are studied at conditions with

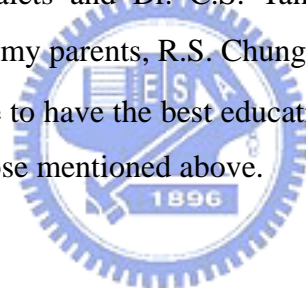
long and short relaxation times. In both conditions, the flux-dependent part is suppressed as increasing the strength of the dephasing. However, the suppression of the flux-independent part only occurs in the long relaxation time condition.

In contrast to the currents, the shot noises of MZ interferometers just reveal the negative value as a result of fermion nature. The low temperature and the low frequency conditions are considered here. In the low temperature condition, the variations of the shot noises are the oscillations with increasing amplitude as increasing the frequency. The different behaviors of the currents and the shot noises with respect to the frequency lead to the regimes where the shot noises exist although the currents vanish. Taking the adiabatic limit, the noiseless regime could be found by tuning two phases, the magnetic phases and the pumping phases. Otherwise, in the low frequency situation, the noiseless condition is also found while removed as taking into account the influence of the temperature.

Finally, a configuration with finger gate array pump is investigated. A pair of finger gate arrays on the top of a narrow wire are staggered and AC biased with the same frequency but differing by a phase. As the finger gates per array are larger than two, the mechanisms of pump currents become the time-dependent Bragg reflection, not just the processes of the photon-assisted interferences. Such explanations are suitable for both the instantaneous and the non-instantaneous regimes.

Acknowledgement

After hard working for years, I am glad that my PhD thesis could be finished and contain many important and interesting findings. Here I show many thanks to my dear partners. First, I would like to thank God. What I could own is the gift from Him. He knows what I need in each moment and gives me the help and the consolation in my difficult time. Second, I thank a lot to my PhD supervisors, Prof. C.Y. Chang (張俊彥) and Prof. C.S. Chu (朱仲夏), and the advisor of GSSAP (graduate student study abroad program), Prof. M. Büttiker. I appreciate Prof. Chang's open attitude for the direction of the research and encourages me to explore the area I feel interested in. I learn two important characters, the care and the patience, on research works from Prof. Chu. The way of Prof. Büttiker to get new ideas of the research work and do the project efficiently makes a great impact on me. I also thank my coworkers, Prof. P. Samuelsson, Prof. M. Moskalets and Dr. C.S. Tang. They help the thesis in an essential way. Finally, I thank my parents, R.S. Chung (鐘如松) and J.E. Liu (劉娟兒). They raise me and support me to have the best education. All of my achievements not only belong to me but also those mentioned above.



Contents

Chapter 1 Introduction

1.1 Introduction to Low Dimensional Systems	p.1
1.2 Motivation	p.2
1.3 Thesis Outline	p.7
References	p.9

Chapter 2 Transport in Voltage Driven Electronic Mach-Zehnder and Hanbury Brown Twiss Interferometers

2.1 Introduction of Electronic Mach-Zehnder and Hanbury Brown Twiss Interferometers	p.16
2.2 Model and Theory	p.20
2.2.1 Optical Analogs in the Quantum Hall Regime	p.20
2.2.2 Scattering Approach to Currents and Noises	p.22
2.2.3 Dephasing Voltage Probe Model	p.23
2.3 Mach-Zehnder Interferometers	p.26
2.3.1 Effects of the Dephasing	p.35
2.4 Hanbury Brown Twiss Interferometers	p.39
2.4.1 Effects of the Dephasing	p.42
2.5 Summary	p.44
References	p.45

Chapter 3 Transport in Quantum Pump Driven Electronic Mach-Zehnder interferometers

3.1	Introduction of Quantum Pump effects	p.63
3.2	Theory and Model	p.65
3.2.1	Floquet Scattering Approach	p.65
3.2.2	Mach Zehnder Interferometers	p.67
3.3	Pumped Currents	p.69
3.3.1	Weak Amplitude Pumping	p.73
3.3.2	Adiabatic, Weak Pumping	p.75
3.3.3	Rectification Effects	p.76
3.4	Dephasing	p.78
3.4.1	Long Charge Relaxation Time $\tau_{RC} \gg T$	p.80
3.4.2	Short Charge Relaxation Time $\tau_{RC} \ll T$	p.81
3.5	Summary	p.83
3.6	Appendix A: Oscillating Barriers	p.85
3.7	Appendix B: Time Representation of Pumped Currents	p.88
3.8	Appendix C: Shot Noises	p.91
	References	p.101

Chapter 4 Finger-Gate Array Quantum Pumps: Characteristics and Mechanisms

4.1	Introduction of Gate Array Pumping	p.115
4.2	FGA pair model	p.116
4.3	Numerical Results	p.118
4.3.1	Single Finger-Gate Pair Case	p.118
4.3.2	Finite Finger-Gate-Array Pair Case	p.120

4.3.2.a	Tuning Back-Gate	p.120
4.3.2.b	Tuning Split-Gate	p.123
4.4	Summary	p.127
	References	p.129
<i>Chapter 5 Conclusions</i>		p.139
Vita (Chinese)		
Publication List		



Figure Captions

Chapter 2

Fig. 2.1 An optical Mach-Zehnder interferometer. A beam of light incident from 1 is split in two partial beams at the semitransparent beam splitter A. The two partial beams acquire geometrical phases ϕ_1 and ϕ_2 respectively and are rejoined at the second beam splitter B. The light intensity is measured in detectors 3 and 4. p.53

Fig. 2.2 The electronic analog of the MZ-interferometer, implemented by Ji et al. [27] in a conductor in the Quantum Hall regime. The electronic reservoir 1 is biased at eV and reservoirs 2 to 4 are kept at ground. The edge states (solid lines) have a direction of transport indicated by arrows. The QPC's A and B play the role of the beam splitters in Fig. 2.1. Geometrical phases ϕ_1 and ϕ_2 and the AB-flux Φ are shown. p.54

Fig. 2.3 Current visibility of the Mach-Zehnder interferometer $v_{I,MZ}$ versus normalized temperature $k_B T/E_c$ for $T_A = T_B$. p.55

Fig. 2.4 Noise visibility $v_{N,MZ}^\ominus$ [figure (a)] of the h/e and $v_{N,MZ}^{2\ominus}$ [figure (b)] of the $h/2e$ oscillations in the shot noise of the Mach-Zehnder interferometer versus transmission T_A of beam splitter A for $E_c \gg k_B T, eV$ for various transmission probabilities T_B of beam splitter B. p.56

Fig. 2.5 Noise visibilities $v_{N,MZ}^\ominus$ (for $T_A, T_B \ll 1$) of the h/e and $v_{N,MZ}^{2\ominus}$ of the $h/2e$ oscillations in the shot noise correlation of a Mach-Zehnder interferometer for $T_A = T_B = 1/2$ versus $k_B T/E_c$ for $eV \ll k_B T, E_c$

(red, thick curve) and versus eV/E_c for $k_B T \ll E_c$, eV (blue, thin curve). p.57

Fig. 2.6 The electrical MZ-interferometer, Fig. 2.2, with a dephasing voltage probe, 5, attached along one edge. p.58

Fig. 2.7 Two-source, four-detector optical Hanbury Brown Twiss geometry proposed in Ref. [33]. Two beams of light incident from 2 and 3 are split in partial beams at the semitransparent beam splitters C and D. The partial beams acquire geometrical phases ϕ_1 to ϕ_4 and are rejoined in the beam splitters A and B. The light intensity is measured in detectors 5 to 8. p.59

Fig. 2.8 Two-source, four-detector electrical Hanbury Brown Twiss geometry implemented in a conductor in the Quantum Hall regime. The electronic reservoirs 2 and 3 biased at eV and reservoirs 1 and 4 to 8 are kept at ground. The edge states (solid lines) have a direction of transport indicated by arrows. The QPC's A and B play the role of the beam splitters in Fig. 2.7. Geometrical phases ϕ_1 to ϕ_4 and the AB-flux Φ are shown. p.60

Fig. 2.9 Noise visibilities $V_{N,HBT}^{\Theta,58}$ and $V_{N,HBT}^{\Theta,57}$ of shot noise correlations in the HBT geometry versus transmission probability T_A for various values of T_B . A symmetric geometry, $E_c \gg kT, eV$, and identical QPC's C and D are considered. p.61

Fig. 2.10 The electrical HBT-interferometer, Fig. 2.8, with a dephasing voltage probe, 9, attached along one edge. p.62

Chapter 3

Fig. 3.1 The pump driven MZI implemented in a conductor in the quantum Hall regime, supporting a single, unidirectional edge state. The conductor is connected to four reservoirs $\alpha = 1$ to 4 kept at the same potential. Two electrostatic split gates, at A and B , are acting as QPCs. The corresponding gate potentials $V_A(t, \phi_A)$ and $V_B(t, \phi_B)$, with ϕ_A and ϕ_B the pumping phases, vary periodically in time. The time dependent potentials give rise to scattering in both real and energy space and are driving the pump current. An Aharonov-Bohm flux Φ threads the MZI. p.108

Fig. 3.2 Two qualitatively different types of first order photon-assisted interference processes contributing to the current: (a) along the same spatial paths L or R and (b) along the different spatial paths L and R. The paths in (b) are sensitive to the enclosed flux Φ . Filled balls indicate inelastic scattering, the electrons pick up or lose one quantum of energy $\hbar\omega$, while empty balls indicate elastic scattering. p.109

Fig. 3.3 The flux independent current $I_3^{(0)}$ (upper panel) and the flux dependent current $I_3^{(\Phi)}$ (lower panel) as a function of pump frequency. Guided by the experiments in Ref. [50], [51], we have taken an asymmetry, $\tau = 5\hbar/E_c$, and symmetric static beam splitters, $a_A = a_B = 1$. The other parameters are $b_A = 0.4, b_B = 1.3$ (strong pumping), $\phi_A = 0$, $\phi_B = 0.8\pi$ and $\psi_{LR} = 0.8\pi$. p.110

Fig. 3.4 The pump driven MZI of Fig. 3.1 with the left arm connected with strength ϵ to a voltage probe φ . The dynamics of the potential V_φ of the probe is governed by the charge relaxation time (see text). p.111

Fig. 3.5 At the low temperature condition $k_B T \ll \hbar\omega$, the variations of the flux-independent part $P_{34}^{(0)}$ and the flux-dependent parts $P_{34}^{(\Phi)}$, $P_{34}^{(2\Phi)}$ of the shot noises (the up panel) and the currents (the down panel) are plotted with respect to the pumping frequency. The parameters are shown in the text. p.112

Fig. 3.6 At the low temperature condition $k_B T \ll \hbar\omega$, the shot noises P_{34} are shown as a function of the phase differences $\phi = \phi_B - \phi_A$ and the magnetic phases Φ/Φ_0 subject to the frequencies (a) $\omega = 15\text{GHz}$ and (b) $\omega = 1.43\text{GHz}$. Contrary to the non-adiabatic, large frequency condition, the noiseless regimes (denoted by triangle) are found at the adiabatic, low frequency condition. Other parameters are shown in the text. p.113

Fig. 3.7 (a) In the adiabatic limit, the current correlations vary with the frequency at the conditions: $k_B T \ll \hbar\omega$ and $\hbar\omega \ll k_B T \ll E_c$ (the second inequality ensures no thermal effects). At the low frequency condition $\hbar\omega \ll k_B T$, we find that (b) the decaying of three parts of current correlations $P_{34}^{(0)}$, $P_{34}^{(\Phi)}$ and $P_{34}^{(2\Phi)}$ with respect to the temperature; (c) contrary to fig. 3(b), at $\phi = 0$ and $\Phi/\Phi_0 = 0.75$ the temperature suppresses the amplitudes of the current correlations and removes the noiseless regime, enlarged in the inset; (d) contrary to fig. 3(b) along $\Phi/\Phi_0 = 0.25$, the cosine behaviors of the current correlations are

smearred as increasing temperature. Other parameters are shown in the text.

p.114

Chapter 4

Fig. 4.1 Top view of the proposed system structure is for the case of FG number $N = 4$. A FGA pair locates on top of a narrow channel. \tilde{V}_i denotes the amplitude of the potential energy and ϕ is the phase difference.

p.132

Fig. 4.2 Total current transmission coefficient versus X_μ for a pair of FG at (a) $\Omega = 0.6 \Delta \varepsilon$ and (b) $\Omega = 0.1 \Delta \varepsilon$. The transmissions of the right-going (left-going) electrons are represented by the solid (dotted) curve. The subband level spacing is $\Delta \varepsilon$. Parameters $\alpha = 1/4$ and $\phi = \pi/2$ are chosen to meet the optimal condition.

p.133

Fig. 4.3 The pumped currents versus X_μ with the same parameters used in Fig. 4.2. The solid and dashed curves correspond, respectively, to $\Omega = 0.6\Delta\varepsilon$ and $\Omega = 0.1\Delta\varepsilon$.

p.134

Fig. 4.4 Total current transmission coefficient versus X_μ for $N = 4$ at (a) $\Omega = 0.6\Delta\varepsilon$ and (b) $\Omega = 0.1\Delta\varepsilon$. The transmissions of the right-going (left-going) electrons are represented by the solid (dotted) curve. The parameters $\alpha = 1/4$ and $\phi = \pi/2$.

p.135

Fig. 4.5 Pumped current versus X_μ . The choices of parameters are the same as in Fig. 4.4. The solid and dashed curves correspond, respectively, to $\Omega = 0.6\Delta\varepsilon$ and $\Omega = 0.1\Delta\varepsilon$.

p.136

Fig. 4.6 The dependence on subband level spacing $\Delta \varepsilon$ of (a) the total current transmission coefficient, and (b) the pumped current. The abscissa is

depicted by Eq. (4.10) where $\mu = 0.049$ and $N = 4$. Pumping frequency $\Omega = 0.0084$ in all curves except for the dotted curve in (b), where $\Omega = 0.0014$. Parameters $\phi = \pi/2$ and $\alpha = 1/4$ for all curves except for the dashed curve in (b), where $\alpha = 1/5$. In (a), the solid (dashed) curve is for $T_{\rightarrow}(X_g)$ [$T_{\leftarrow}(X_g)$], and contributions from the second Fourier component of $V(x, t)$ are indicated by arrows.

p.137

